AGU PUBLICATIONS

JGR

Journal of Geophysical Research: Oceans

RESEARCH ARTICLE

10.1002/2013JC009657

Special Section:
The 2011-12 Indian Ocean Field Campaign: Atmospheric-Oceanic Processes and MJO Initiation

Seaglider observations of equatorial Indian Ocean Rossby waves associated with the Madden-Julian Oscillation

Benjamin G. M. Webber[1], Adrian J. Matthews[1,2], Karen J. Heywood[1], Jan Kaiser[1], and Sunke Schmidtko[1,3]

[1]Centre for Ocean and Atmospheric Sciences, School of Environmental Sciences, University of East Anglia, Norwich, UK, [2]Centre for Ocean and Atmospheric Sciences, School of Mathematics, University of East Anglia, Norwich, UK, [3]Helmhotz Centre for Ocean Research - GEOMAR, Kiel, Germany

Key Points:
- Ocean Rossby waves associated with the MJO observed at unprecedented resolution
- New mechanism for the MJO to drive variations in primary productivity identified
- Capacity of gliders to observe these waves demonstrated

Correspondence to:
B. G. M. Webber,
b.webber@uea.ac.uk

Citation:
Webber, B. G. M., A. J. Matthews, K. J. Heywood, J. Kaiser, and S. Schmidtko (2014), Seaglider observations of equatorial Indian Ocean Rossby waves associated with the Madden-Julian Oscillation, *J. Geophys. Res. Oceans*, *119*, 3714–3731, doi:10.1002/2013JC009657.

Received 25 NOV 2013
Accepted 21 MAY 2014
Accepted article online 26 MAY 2014
Published online 12 JUN 2014

Abstract During the CINDY–DYNAMO field campaign of September 2011–January 2012, a Seaglider was deployed at 80°E and completed 10 north-south sections between 3 and 4°S, measuring temperature, salinity, dissolved oxygen concentration, and chlorophyll fluorescence. These high-resolution subsurface observations provide insight into equatorial ocean Rossby wave activity forced by three Madden-Julian Oscillation (MJO) events during this time period. These Rossby waves generate variability in temperature O(1°C), salinity O(0.2 g kg^{-1}), density O(0.2 kg m^{-3}), and oxygen concentration O(10 μmol kg^{-1}), associated with 10 m vertical displacements of the thermocline. The variability extends down to 1000 m, the greatest depth of the Seaglider observations, highlighting the importance of surface forcing for the deep equatorial ocean. The temperature variability observed by the Seaglider is greater than that simulated in the ECCO-JPL reanalysis, especially at depth. There is also marked variability in chlorophyll fluorescence at the surface and at the depth of the chlorophyll maximum. Upwelling from Rossby waves and local wind stress curl leads to an enhanced shoaling of the chlorophyll maximum by 10–25 m in response to the increased availability of nutrients and light. This influence of the MJO on primary production via equatorial ocean Rossby waves has not previously been recognized.

1. Introduction

CINDY (Cooperative Indian Ocean Experiment on Intraseasonal Variability in Year 2011)–DYNAMO (DYNAmics of the Madden-Julian Oscillation; the US participation in CINDY) was a collaborative international effort to understand the processes that are associated with the initiation and propagation of the Madden-Julian Oscillation (MJO) in the Indian Ocean (see *Yoneyama et al*. [2013] for a summary). At the core of the program was an intensive field campaign in late 2011–early 2012 to collect in situ observations. The campaign consisted mainly of radar surveys from ships and island sites, shipborne observations of atmospheric and oceanic properties [*Gottschalck et al*., 2013; *Moum et al*., 2013], enhanced mooring arrays and aircraft surveys, as well as modeling studies [*Fu et al*., 2013]. As part of this observational field campaign, we deployed a Seaglider in the central equatorial Indian Ocean for a period of 4 months, with the intention of observing oceanic Rossby waves associated with the MJO.

The MJO is the dominant cause of atmospheric intraseasonal variability in the tropics [*Madden and Julian*, 1971, 1972]. It is associated with convective rainfall and wind variability with a periodicity of around 30–60 days, although its quasiperiodic nature generates a spectral signal with power extending to 95 days for convection [*Salby and Hendon*, 1994]. See *Zhang* [2005] and *Lau and Waliser* [2005] for full reviews of the MJO and its impacts.

Equatorial ocean waves dominate the dynamics of the tropical oceans on time scales from intraseasonal [*Hendon et al*., 1998] to interannual [*McPhaden*, 1999]. They can be forced by anomalies in surface wind and buoyancy forcing, or through the reflection of other waves at meridionally orientated coastlines. At intraseasonal time scales, the MJO forces equatorial Kelvin and Rossby waves in all the tropical ocean basins [*Webber et al*., 2010]. Observations suggest that the MJO generates oceanic equatorial Kelvin waves that can trigger or amplify ENSO events [*McPhaden*, 1999]. There is also growing evidence of the potential for oceanic equatorial Rossby waves in the Indian Ocean to force variability in the MJO [*Webber et al*., 2010, 2012a, 2012b], and for feedbacks between the two [*Han et al*., 2001].

These waves modify the upper ocean heat content and the mixing of the cold subsurface water, leading to changes in sea surface temperature (SST) [*McCreary*, 1983]. Equatorial Kelvin and Rossby waves can alter the climate due to their impact on SST [*Kessler and McPhaden*, 1995], and modulate biological activity through upwelling and downwelling that modify the supply of nutrients to the near-surface waters [*Uz et al*., 2001]. However, *Dandonneau et al*. [2003] found apparent chlorophyll maxima in Rossby wave-induced downwelling zones, and hypothesized that the ocean color signal was due to the convergence of floating ecosystem by-products, so it is important to verify the location of any chlorophyll signal in relation to vertical motion. It is possible to observe the impact of Rossby waves on surface chlorophyll-*a* variability from satellite data [*Heywood et al*., 1994], enabling studies of chlorophyll variability across broad spatial and temporal scales. It is known that the MJO influences chlorophyll concentrations [*Waliser et al*., 2005] through modulation of the thermocline depth, wind stress, and upwelling, and that the western equatorial Indian Ocean has strong chlorophyll variability [*Dandonneau et al*., 2004]. However, the MJO-induced Rossby waves remain poorly studied, especially in terms of high-resolution observations of their vertical structure and their impact on biogeochemistry.

In this study, we use a Seaglider [*Eriksen et al*., 2001] to study the ocean variability that occurs in response to equatorial ocean Rossby waves associated with the MJO. We consider both the variability associated with upwelling and downwelling of physical properties, as well as the impact of nutrient upwelling on chlorophyll concentrations. The use of a Seaglider allows us to study these waves with high vertical resolution over a period of approximately 4 months. Section 2 describes the MJO variability and the surface features of the Rossby waves that result. Section 3 discusses the observations gathered by the Seaglider and the mean vertical structure from these observations is documented in section 4. Section 5 describes the observed Rossby waves and the subsequent effects on chlorophyll concentration. The conclusions are presented in section 6.

2. The MJO and Planetary Waves

2.1. Data

Sea level anomaly (SLA) data from the merged Ocean Topography Experiment (TOPEX)/Poseidon-Earth Remote Sensing (T/P-ERS) satellite altimetry product, available from AVISO [*Fu et al*., 1994], were used to diagnose ocean Rossby waves. Weekly data on a $0.25^\circ \times 0.25^\circ$ grid were interpolated to daily values using cubic splines. Outgoing long-wave radiation (OLR) was used as a proxy for tropical deep convective precipitation since the cold, high tops of convective clouds emit low values of OLR. The OLR data were obtained as $2.5^\circ \times 2.5^\circ$ resolution gridded daily values [*Liebmann and Smith*, 1996]. Surface wind data were obtained from the ERA-interim reanalysis product [*Dee et al*., 2011]. We also use oceanographic data from the ECCO (Estimating the Circulation and Climate of the Ocean-Global Ocean Data Assimilation Experiment; *Wunsch and Heimbach* [2007])-JPL ocean reanalysis.

The SLA, OLR, wind, and ECCO-JPL data were all obtained over the longest period for which each data set was available to facilitate accurate estimation of the trend and mean annual cycle, which were both subtracted from the original data to produce anomalies. The SLA data were obtained from October 1992 to February 2012, the OLR and wind data from January 1979 to May 2012, and the ECCO-JPL data from January 1993 to July 2012. To isolate the intraseasonal signals, the calculated daily anomalies were then band-pass filtered using a 20–200 day Lanczos filter, using 61 symmetric weights such that the filtered data were curtailed by 30 days of data at each end compared with the original.

2.2. MJO and Rossby Waves During CINDY–DYNAMO

There were three distinct MJO cyclesduring the CINDY–DYNAMO period [*Gottschalck et al*., 2013], with their active convective phases defined by the three eastward-propagating equatorial negative OLR anomalies between October and December 2011. These are shown in Figure 1a by diagonal dashed red lines with a slope equal to the canonical MJO propagation speed of 5 m s^{-1} [*Zhang*, 2005], passing through minima in OLR at the longitude of the Seaglider (78.8°E). These active convective events were followed by progressively stronger westerly wind events in the equatorial Indian Ocean (Figure 1b).

In order to assess the equatorial wave activity during this period, we have projected the SLA onto the meridional structures of the Kelvin and first meridional mode Rossby waves. We have also examined the

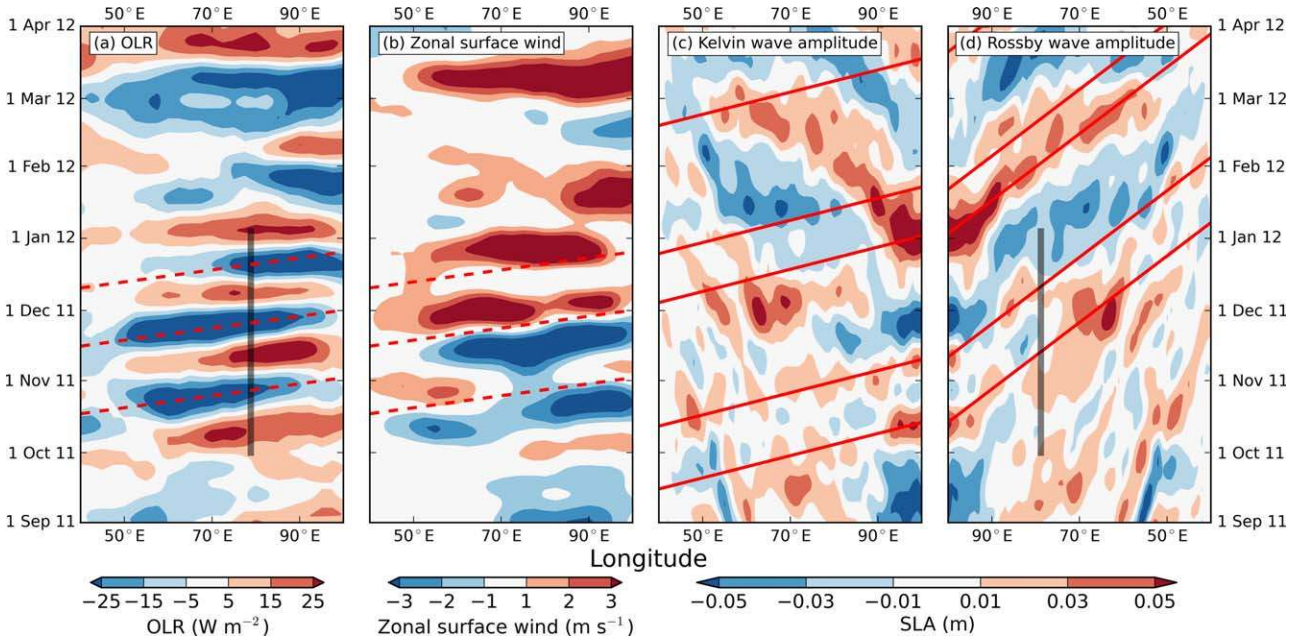

Figure 1. Hovmöller diagrams of anomalies of (a) outgoing longwave radiation (OLR) averaged between 10°S and 10°N; (b) Zonal surface wind averaged over 10°S–10°N; (c) Projection of SLA onto the meridional structure of a Kelvin wave with speed c=2.7 m s^{-1}; (d) Projection of SLA onto the meridional structure of a first meridional mode Rossby wave with speed c/3 = 0.9 m s^{-1}. The vertical black lines in (a) and (d) represent the location of the Seaglider, the diagonal dashed red lines in (a) (reproduced in (b)) indicate the active MJO events (phase speed of 5 m s^{-1} linked to SLA minima at the Seaglider location); the diagonal solid red lines in (c) and (d) indicate the phase speed of the Kelvin and Rossby waves linked to amplitude maxima at the eastern boundary (100°E).

combined projection onto the superposition of the Kelvin and Rossby wave structure; as expected, the output is a linear combination of the two projections and is very similar to the average sea surface height between 5°N and 5°S.

We first analyze the Kelvin wave activity, since this is known to be directly forced by westerly wind bursts associated with the MJO [*Hendon et al.*, 1998; *Webber et al.*, 2010]. The normalized meridional structure of SLA associated with an equatorial ocean Kelvin wave [*Delcroix et al.*, 1994] is given by

$$h = 2^{-1/2}\pi^{-1/4}\exp\left(\frac{\beta y^2}{2c}\right) \quad (1)$$

where y is the meridional coordinate, β is the meridional gradient of the Coriolis parameter, and c is the Kelvin wave phase speed, for which we use 2.7 m s^{-1} following *Chelton et al.* [1998]. The resulting structure is shown as the black line in Figure 2a. We project the intraseasonally filtered SLA onto this meridional structure to diagnose the Kelvin wave amplitude (Figure 1c). Note that we impose no constraint on the propagation of these anomalies, so a further check is to examine the phase speed of the anomalies. The slope of the diagonal red lines in this figure is set by the phase speed c, and their position in time is linked to maxima in the wave amplitude at the eastern boundary (100°E). These phase lines clearly match the propagation speed of the Kelvin wave signals, although the Rossby waves also project onto this signal, particularly during January and February when the Rossby wave activity is particularly strong. This overlap is not surprising given that both the Kelvin wave and the first meridional mode Rossby wave have positive anomalies at the equator.

The Kelvin wave signals appear to follow westerly wind bursts associated with the MJO events (Figures 1–1c), although the broad peak in the Kelvin wave signal at the eastern boundary from mid December to late January can be linked to a succession of westerly wind anomalies at that time. To quantify the relationship between wind forcing and the Kelvin waves, we integrate the intraseasonal wind stress onto the Kelvin wave characteristic following *Hendon et al.* [1998]. The relationship between this integral and the projected

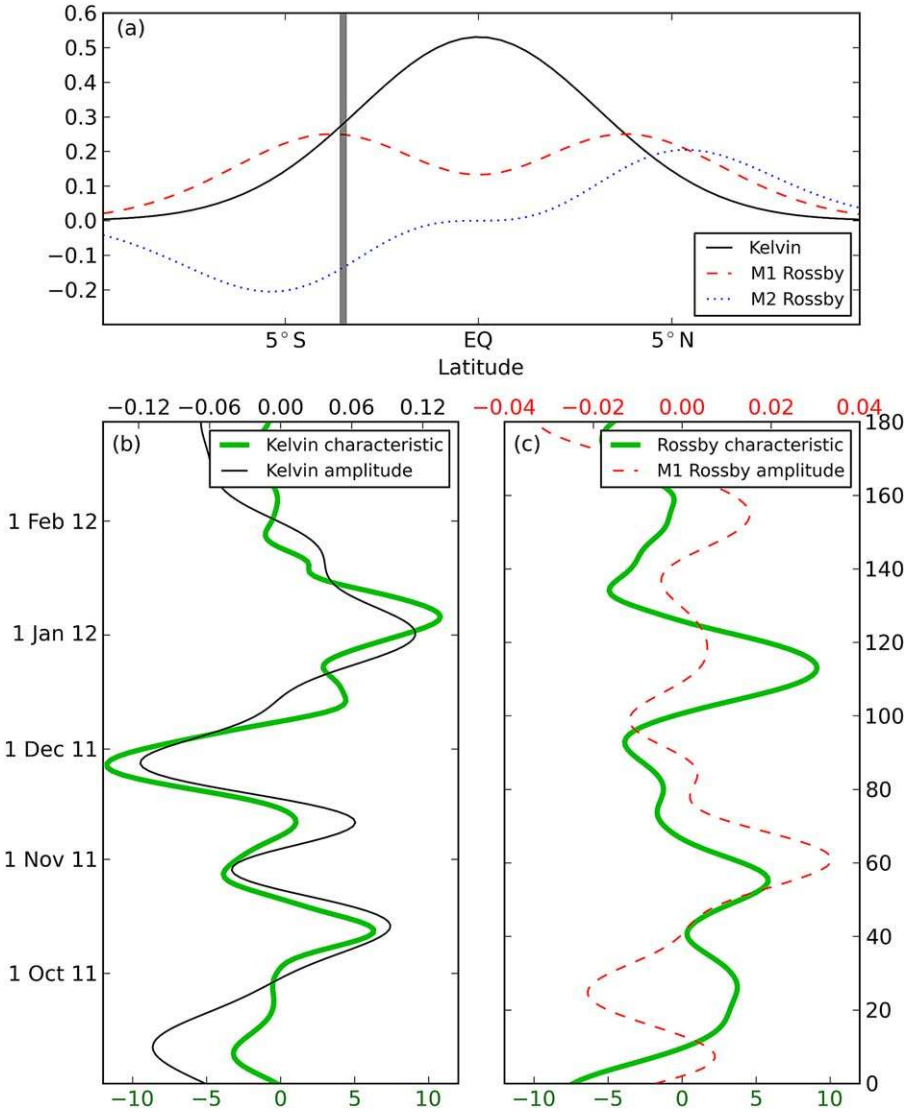

Figure 2. (a) Theoretical latitudinal sea surface height structure of a Kelvin wave (black line) with phase speed 2.7 m s^{-1}, and the corresponding first (red dashed line) and second (blue dotted line) meridional mode Rossby waves; (b) The Kelvin wave amplitude diagnosed from the projected SLA at 100°E (green line) and the thermocline depth anomaly calculated from the integration of the surface wind forcing along the Kelvin wave characteristic (black line); (c) The first meridional Rossby wave amplitude diagnosed from the projected SLA at 100°E (green line) and the thermocline depth anomaly calculated from the integration of the surface wind forcing along the Kelvin wave characteristic (black line)

Kelvin wave amplitude at the eastern boundary is very strong (Figure 2b; $r = 0.82$), suggesting that the majority of the Kelvin wave signal at 100°E can be explained by this integrated wind forcing.

The meridional structure of SLA associated with the first meridional mode Rossby wave (Figure 2a, red dashed line) is given by

$$h = 2^{-3/2}\pi^{-1/4}\exp\left(\frac{-\beta y^2}{2c}\right)\left(\frac{\beta y^2}{c}+\frac{1}{2}\right) \quad (2)$$

The projection of intraseasonal SLA onto this structure is shown in Figure 1d, with diagonal lines calculated in the same manner as for the Kelvin waves (linked to Rossby wave maxima at 100°E). It is clear that Rossby wave maxima at the eastern boundary closely follow Kelvin wave maxima at the same location, and anomalies can be seen propagating westwards from these, indicative of reflection here as seen in composites of

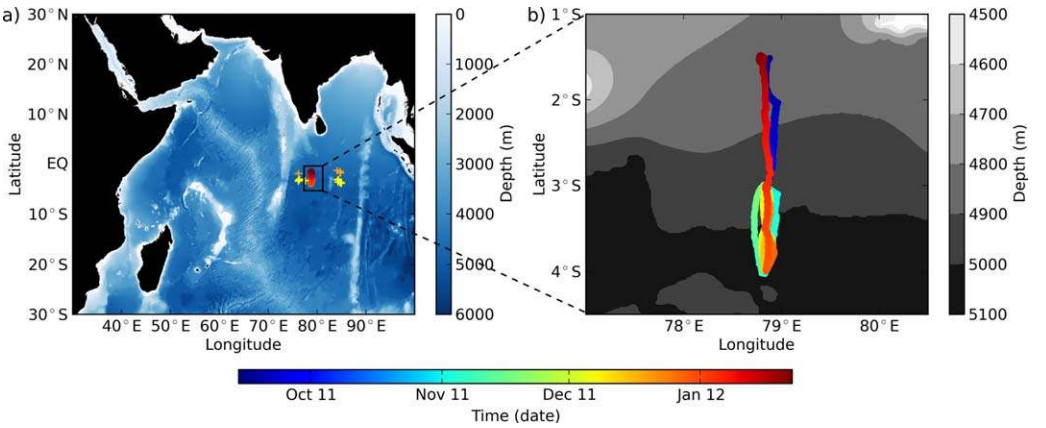

Figure 3. Bathymetry of the Indian Ocean (grayscale) and location of the Seaglider (scatter points), colored by time (see legend). Orange and yellow crosses in (a) indicate the location of Argo profiles used for comparison with the Seaglider data at the deployment and section locations, respectively.

the MJO [*Oliver and Thompson*, 2010; *Webber et al*., 2010]. However, many of these signals do not propagate coherently across the width of the Indian Ocean. We project the wind stress onto the characteristic of the first meridional mode equatorial Rossby wave [*Delcroix et al*., 1994], but the match between this and the Rossby wave integral at the western boundary is not particularly close (Figure 2; $r = 0.26$). Nor is there a good match at the longitude of the Seaglider deployment (not shown). Therefore, it appears that the Rossby wave signal is a combination of freely propagating waves and waves forced by local wind stress. This is apparent in the rapid propagation of the negative Rossby wave signal during January 2012, which can be linked to the preceding westerly winds across the width of the basin during late December 2011.

In February-March 2012, a very intense MJO event is triggered [*Gottschalck et al*., 2013; *Shinoda et al*., 2013], the beginning of which can be seen in Figure 1a. The coincidence of the initiation of this event and the arrival of the downwelling Rossby wave in the central Indian Ocean during late February 2012 has been discussed by *Shinoda et al*. [2013]. It appears to be a combination of the Kelvin wave signals associated with the latter two of these three MJO cycles that triggered this Rossby wave through reflection at the eastern boundary of the Indian Ocean. If this is indeed the case, then it suggests an oceanic connection between the MJO activity during the CINDY–DYNAMO period and the major MJO event triggered in February 2012, consistent with the triggering mechanism proposed by *Webber et al*. [2012a].

3. Seaglider Observations

3.1. Measurements

In association with the CINDY–DYNAMO field campaign, a Seaglider was deployed from the R/V Roger Revelle to patrol between 3° and 4°S (Figure 3), the latitude of the strongest signals associated with equatorial Rossby waves [*Webber et al*., 2010]. The Seaglider completed 10 sections between 3 and 4°S over a period of 96 days from 1 October 2011 to 4 January 2012. Due to ballasting problems, the progress of the Seaglider was initially slower than ideal, particularly for the first northwards section which took 20 days in total as the glider was advected off course by currents and eddies. The trim of the Seaglider was subsequently improved and later sections were completed in around 10 days.

The location of the Seaglider is shown by the thick gray line in Figure 1d, giving an indication of the Rossby wave signals that were observed by the Seaglider. During its deployment, several Rossby wave features are evident. At the start of October 2011, the tail end of a downwelling wave (positive amplitude) was propagating through the region, immediately followed by a weak upwelling signal. This was followed by largely positive SLA, indicative of a downwelling wave, before the start of a strong upwelling wave that passed through in January 2012. We discuss the Rossby wave signal further in section 5.3.

The instruments mounted on the Seaglider for this mission were: a Seabird SBE13 conductivity-temperature (CT) sensor; an Aanderaa 4330 oxygen optode; and a Wetlabs EcoPuck measuring chlorophyll fluorescence.

Pressure drift and hysteresis in the pressure sensor were corrected for. The Seaglider hydrodynamic model [*Frajka-Williams et al*., 2011] was used to correct for the thermal lag of the CT sensor [*Morison et al*., 1994], and data were only used when a minimum vertical velocity threshold of 0.05 m s^{-1} was reached, to ensure that the sensor was well-flushed. Vertical velocity is used instead of total velocity for this threshold since vertical velocity can be directly measured through pressure changes and does not depend on the accuracy of the hydrodynamic model. Spikes in the data are initially removed based on broad tolerances, after which the thermal mass of the sensors is accounted for and the resultant bias removed. We then apply a subjective despiking algorithm to remove outliers in $\Theta - S_A$ space. Any remaining poor-quality data were given a very low weighting in the later optimal interpolation routines.

Temperature and salinity measurements were taken continuously throughout the mission, whereas oxygen and chlorophyll measurements were taken sporadically to conserve battery life; chlorophyll in particular was sampled infrequently, with the average gap between profiles being 3 days. Temperature and salinity were sampled approximately every 5 s (0.5 m vertical resolution) at depths shallower than 300 m, and every 15 s at 300–1000 m (1.5 m vertical resolution). Oxygen concentration was sampled every 5 s at depths shallower than 100 m (200 m when chlorophyll measurements were being taken), then every 15 s to 300 m and every 45 s to 1000 m (4.5 m vertical resolution). The chlorophyll fluorescence was sampled every 15 s to 200 (occasionally 300) m when on, and was switched off below that depth.

A standard procedure for calibration of sensors on ocean gliders is yet to be fully established. All the instruments were factory calibrated less than 2 years before deployment, and the temperature, salinity, and chlorophyll sensors were calibrated less than a year before deployment. Ship CTD casts for calibration were made at the deployment and recovery of the Seaglider for this mission; however, it was impractical to make such a CTD cast at exactly the same location and time as the glider makes a dive, so it is difficult to distinguish between instrument error and differences due to internal waves or spatiotemporal gradients. For this mission, this was exacerbated by a leak in the CT-cell near the end of the mission; all data affected were removed, but the temperature and salinity data could not be compared against the recovery CTD cast. As a result, the CTD casts are only used to check for large offsets in the measurements, with Argo float profiles used as an independent quality check. Water samples for calibration of the dissolved oxygen and chlorophyll sensors were not taken, so the manufacturers' calibrations were used. Note that throughout this paper temperature and salinity data are converted to conservative temperature (Θ) and absolute salinity (S_A), respectively, following *IOC, SCOR, IAPSO* [2010].

We compare the Seaglider data with the ECCO-JPL ocean state estimate, obtained through data assimilation of a wide variety of observations using the adjoint method [*Wunsch and Heimbach*, 2007]. Comparison between the ECCO state estimate and altimetry from the TOPEX-POSEIDON mission showed good agreement in the open ocean regions but poor agreement in areas of strong variability such as coastal regions and parts of the Southern Ocean. Limitations of the state estimate include the scarcity of subsurface observations and the relatively coarse resolution (1° horizontal and 23 vertical levels), meaning that some processes may not be adequately resolved.

To remove the annual cycle from the Seaglider data, we use the monthly isopycnal/mixed-layer ocean climatology (MIMOC) dataset [*Schmidtko et al*., 2013]. This uses all available hydrographic observations to construct a seasonal cycle using optimal interpolation [*Bretherton et al*., 1976]. The radii of influence for the optimal interpolation are 330 km in the horizontal and 45 days in time. The horizontal weighting is adjusted based on a fast-marching algorithm tuned to represent the tendency for ocean properties to correlate along isobaths. In addition, the weights are adjusted to preserve oceanographic fronts and observations prior to 2007 are down-weighted. A major advantage of this climatology for the present study is that it preserves the stratification in regions of strong Rossby wave variability, where conventional isobaric climatologies would smear out the pycnocline.

4. Mean Conditions

4.1. Comparison With CTD Casts

The mean state of the ocean as observed by the Seaglider was analyzed to give context to the discussion of the anomalies that follow, and compare the Seaglider data with other available observations to identify possible biases and offsets in the data. Because of the CT-cell leak near the end of the mission, only the

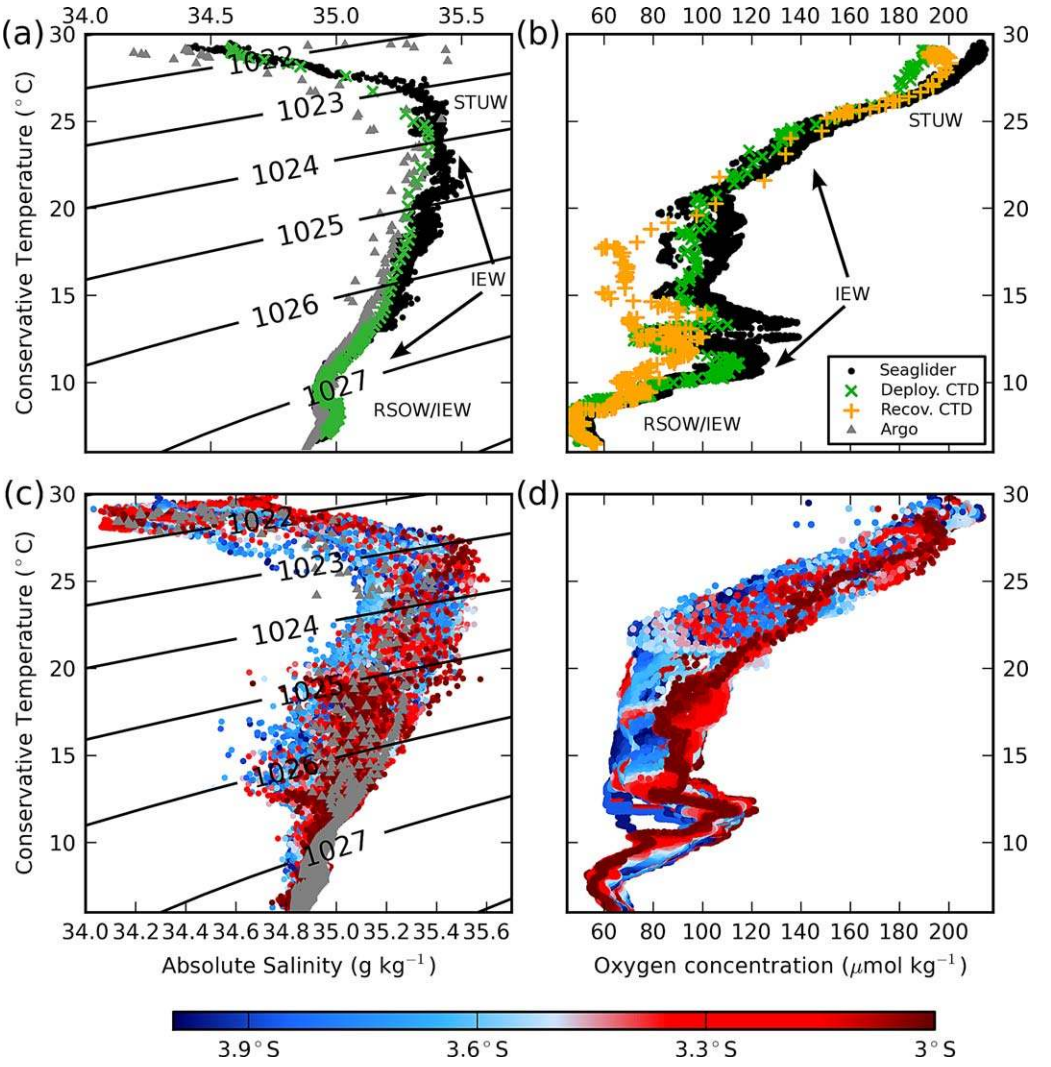

Figure 4. (a) Conservative temperature-absolute salinity diagram for Seaglider observations north of 2°S (black circles), Argo observations within 1°–2° S, 75–85° E (gray triangles), and the calibration CTD casts at the deployment (green cross symbols), and recovery (orange plus symbols); potential density is contoured. (b) Conservative temperature-dissolved oxygen diagram for Seaglider observations in the deployment/recovery region north of 2° S (black circles), and the calibration CTD casts at the deployment (green cross symbols) and recovery (orange plus symbols). (c,d) As (a,b) but for Seaglider and Argo observations between 3–4° S, colored by latitude; the calibration cast data are not shown. The abbreviations STUW, IEW, and RSOW refer to Subtropical UnderWater, Indian Equatorial Water, and Red-Sea Overflow Water, respectively. All plots contain measurements taken between the surface and 1000 m depth.

deployment CTD cast can be usefully compared with the glider data. We use the period when the Seaglider was north of 2°S to enable a comparison that is not overly affected by meridional gradients. The Seaglider temperature and salinity measurements compared well with data from the deployment CTD and with all available Argo profiles (Figure 4a) within 10° longitude and 1° latitude of the region during the time frame of the deployment (yellow crosses in Figure 3a). Because of the broad region from which the Argo data are drawn, an exact agreement is not expected, and differences in float calibration may also account for some discrepancy. At temperatures below 15°C (equivalent to depths greater than 150 m; see section 4), the Argo data overlap both the deployment and recovery CTD and the Seaglider data from the deployment period. Within the thermocline, between temperatures of 15°C and 25°C, there appears to be a bias such that the Seaglider data are warmer and more saline that the Argo and CTD data by up to 2°C or 0.2 g kg^{-1}, respectively. Note that the Seaglider and CTD data were separated by at least 2 km horizontally, and due to the relatively short time taken for the CTD cast, there were few data taken at the same time (the Seaglider was between 290 and 400 m depth during the CTD cast). Therefore, these offsets may simply represent spatial variability. Within the region where the Seaglider performed its repeat N-S sections (between 3° and 4°S),

the glider data exhibit a spread that encompasses the Argo data and no offset is evident (Figure 4c), so no offset was applied to either the temperature or salinity data.

The structure of the Seaglider oxygen concentration generally compared well with the CTD data (Figure 4b). The recovery CTD data (orange + symbols) indicate lower oxygen concentrations between 10 and 20°C when compared with the Seaglider and deployment CTD cast; it seems likely that this is indicative of spatial variability. There is good agreement between the deployment CTD and the Seaglider oxygen data, except for the near surface data, where the Seaglider data suggest higher concentrations. This is most likely to be a calibration issue, but since the CTD data were not calibrated against bottle samples, it is impossible to know the true values. Since we are primarily interested in variability rather than absolute values, this is not critical for this study. The latitudinal variability of the oxygen data (Figure 4d) suggests that there is a tendency for higher oxygen concentrations toward the north in the warmer water (temperatures greater than 10°C), and the opposite in the colder water. However, this is not true everywhere, with some higher concentrations measured at the southern end of the section and vice-versa. The temporal variability of the oxygen sensor was also investigated, with little or no drift found (not shown), therefore no correction for offset or drift was made for the oxygen data.

4.2. Vertical Structure and Water Masses

The mean profile of the water column is a factor in the structure and propagation of the oceanic equatorial Rossby waves, and in the anomalies that result from the Rossby wave-induced circulation. Also, the mean profile can be related to known water mass characteristics to infer its origin.

To diagnose the mean structure, we first gridded the data. To do this, we performed an optimal interpolation [*Bretherton et al*., 1976] of the data to produce a data set at regularly spaced time t_j, depth z_j, and latitude λ_j points. For each gridded variable α_j, a Gaussian weighting function w_{ij} was used to calculate the weighting that each observation α_i contributes to the gridded value:

$$w_{ij}=\exp\left\{-\left[\left(\frac{t_i-t_j}{t_r}\right)^2+\left(\frac{z_i-z_j}{z_r}\right)^2+\left(\frac{\lambda_i-\lambda_j}{\lambda_r}\right)^2\right]\right\}. \tag{3}$$

The radii of influence, t_r, z_r, and λ_r in time, depth, and latitude were chosen to reflect the scales of variability in the processes we are interested in, and the inherent resolution of the observational data. Internal waves and other high-frequency variability can be aliased in glider data due to the slow speed (about 20 cm s^{-1}) of the glider, but this can be overcome by averaging over spatial scales greater than 30 km [*Rudnick and Cole*, 2011]. Since we used a radius in time of $t_r = 5$ days, this is unlikely to affect our results. The radius of influence in depth was z_r=1 m. We used a radius of influence in latitude of $\lambda_r = 0.05°$ (approx 5 km) and then removed the (latitude-dependent) annual cycle before performing an arithmetic meridional average, which will also have removed any internal wave effects. Note that using a larger radius of influence in latitude has the potential to introduce biases toward either end of the section due to the limited domain and large meridional mean gradient.

The background field calculated above was used as the input to the optimal interpolation scheme. The covariances of the data were parameterized using the same Gaussian function (equation (3)) to calculate the analysis increment, which was then added to the background field to create the final optimally interpolated field.

We calculate the mean vertical structure of the observations by arithmetically averaging the optimally interpolated data in time and latitude. These vertical profiles are compared with the Θ-S_A diagrams to reveal features of the mean structure. The main thermocline (30–200 m; Figure 5a) and halocline (30–80 m; Figure 5c) are shallow. There is a distinct salinity maximum at 80 m (Figure 5c). This salinity maximum is also prominent in the Θ-S_A diagram (Figure 4a), and is associated with the presence of Subtropical Underwater (STUW), which originates from the subtropical gyres where evaporation exceeds precipitation; in contrast, the low surface salinity is due to the local dominance of precipitation [*Talley et al*., 2011]. The near-surface density structure (Figure 5b) reflects the structure in temperature and salinity, with the maximum density gradient deeper than the maximum salinity gradient and shallower than the maximum temperature

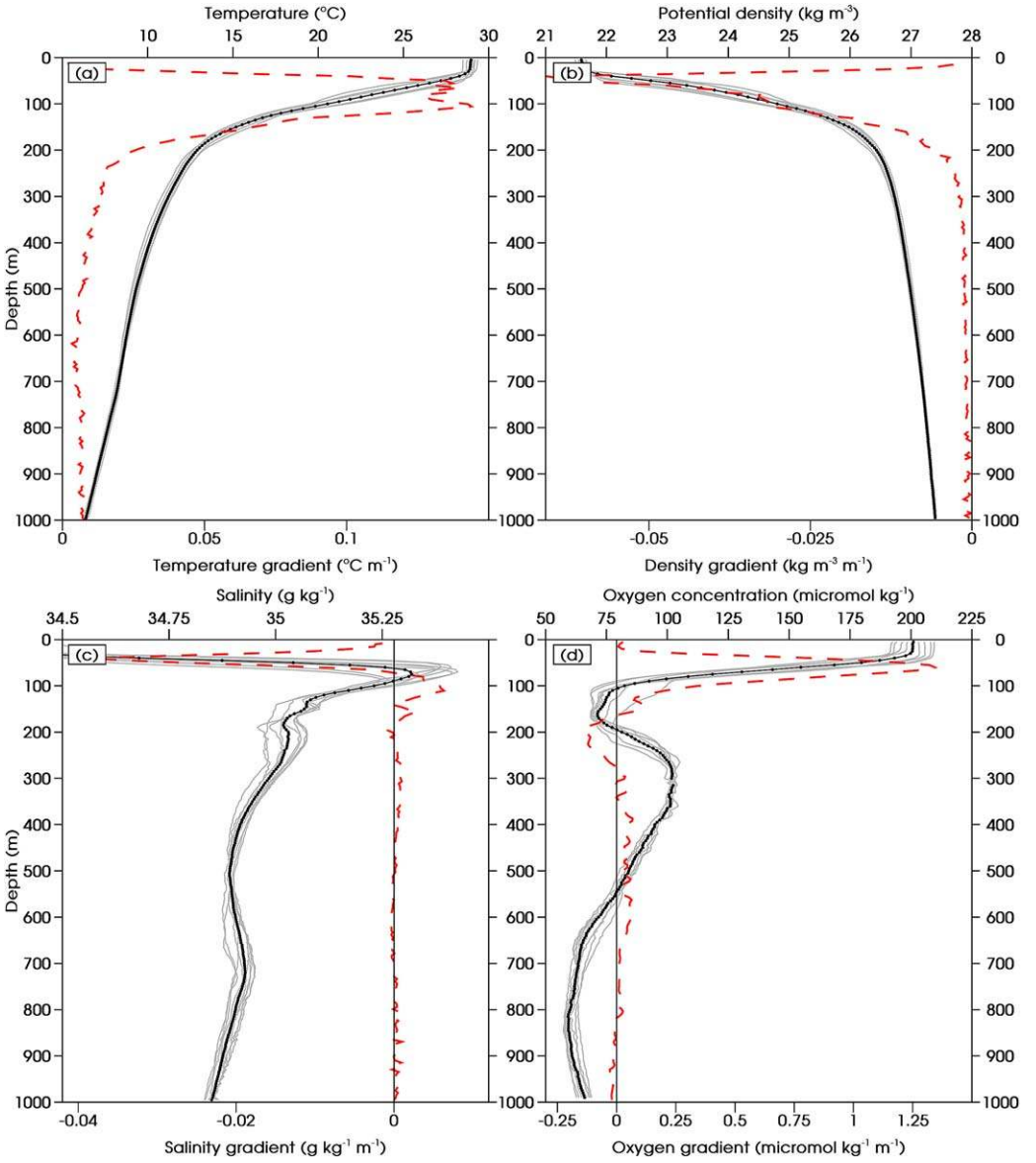

Figure 5. Time and latitudinal average vertical structures from optimally-interpolated Seaglider observations, along with the mean from each N-S section (gray), and the vertical gradient (red dashed). (a) temperature (°C), (b) potential density (kg m^{-3}), (c) absolute salinity (g kg^{-1}), (d) dissolved oxygen concentration (μmol kg^{-1}).

gradient. The Θ-S_A profile within the thermocline (15–30°C) is fairly typical of Indian Equatorial Water (IEW), with salinities between 34.5 and 36 g kg^{-1} [*Talley et al.*, 2011].

The oxygen concentrations observed (Figure 4b) are also consistent with this definition of IEW, showing the characteristic maximum of around 120 μmol kg^{-1} at around 10–12°C (Figure 4b; equivalent to 300 m, Figure 5d), a minimum concentration of around 60 μmol kg^{-1} at 6°C (equivalent to 850 m) and a pronounced oxycline above the 20°C isotherm. The maximum vertical gradient is 1.3 μmol kg^{-1} m^{-1} at around 80 m depth (Figure 5d).

The local salinity maximum that occurs between 700 and 800 m depth (Figure 5c; around 6°C in Figure 4a) is characteristic of Red Sea Overflow Water (RSOW) that has been well-mixed away from its source region, although this signal is weaker here than further to the east [*Talley et al.*, 2011]. The oxygen minimum at these depths is found in profiles of RSOW and IEW; the minimum concentration of around 60 μmol kg^{-1} is in between the minima associated with these water masses, suggesting a mix of the two.

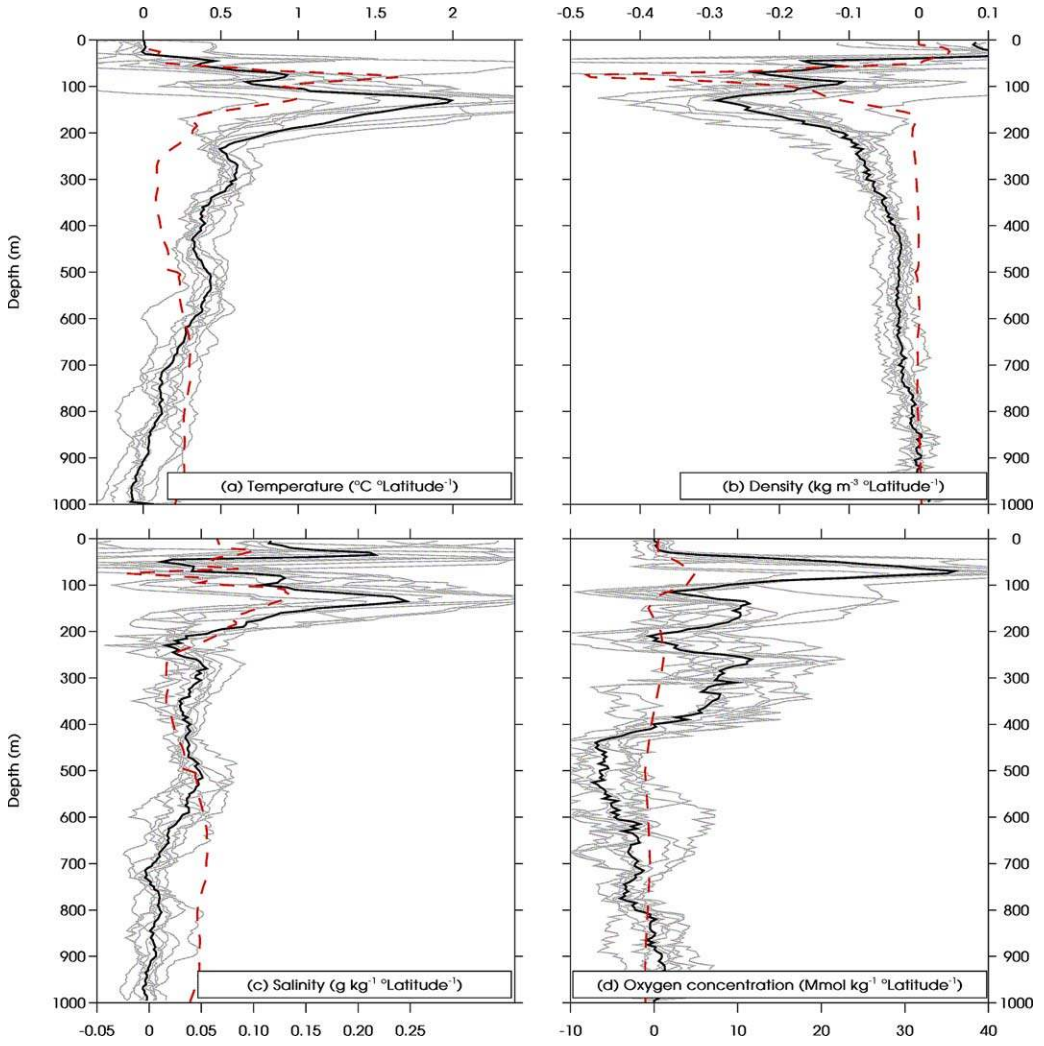

Figure 6. Horizontal gradients of the optimally interpolated data. (a) temperature (°C °Latitude^{-1}), (b) salinity (g Kg^{-1} °Latitude^{-1}), (c) density (Kg m^{-3} °Latitude^{-1}), and (d) oxygen saturation (μmol Kg^{-1} °Latitude^{-1}).

4.3. Meridional Structure

Figure 6 shows the meridional gradients in temperature, density, salinity, and oxygen from the gridded data between 3° and 4° S. It is clear that there are large gradients in all these variables. The strongest meridional gradients in temperature, density, and salinity are all collocated at a depth of around 150 m, just below the thermocline. These meridional gradients are due to a combination of the influence of Indonesian Throughflow (ISW) water to the south, and to increased upwelling and precipitation in the region of the Intertropical Convergence Zone [*Talley et al*., 2011]. However, the gradients are stronger this year than on average; for salinity, the peak gradient is 0.1 g Kg^{-1} larger than in the MIMOC climatology data. For temperature, the gradient at 150 m is almost 1°C/°latitude greater than in the MIMOC climatology, but the meridional gradient at shallower depths is comparable.

5. Rossby Waves

5.1. Observed Anomalies

Having established the mean vertical structure, we now turn our attention to the anomalies from this, particularly to observe the signal of ocean Rossby waves propagating through the study region. Negative SLA is associated with upwelling Rossby waves and a shoaling of the thermocline while the opposite is true for

positive SLA. We examine the depth of the 20°C isotherm from gridded Seaglider data since this quantity is commonly used as an indicator of thermocline variability [*Kessler et al*., 1995]. Here, we calculate it by meridionally averaging the optimally interpolated temperature data to obtain a relationship between temperature and depth and then linearly interpolate between temperature values to determine the depth of the 20°C surface at each time point.

We project the intraseasonal SLA onto both the first and second meridional mode Rossby wave structure, then compare these signals to the depth of the 20°C isotherm calculated from the Seaglider data (Figure 7a). We also compute the upwelling induced by Ekman pumping from the curl of the wind stress as follows

$$w_E = \frac{\hat{\mathbf{k}} \cdot (\nabla \times \tau)}{\rho f} \tag{4}$$

where $\hat{\mathbf{k}} \cdot (\nabla \times \tau)$ denotes the horizontal curl of the wind stress τ, $\rho = 1024$ kg m^{-3} is a representative density of water in the Ekman layer, and $f = 8.9 \times 10^{-6}$ s^{-1} is the Coriolis parameter at 3.5°S. We calculate the cumulative Ekman upwelling, starting from zero on 11 October 2011 (red dashed line in Figure 7a), which would be expected to match the isotherm depth if this was the main cause of thermocline variability. However, the relationship is weak, other than during late December and early January, when a particularly strong downwelling event (c.f. instantaneous upwelling Figure 7b, blue dotted line) leads to a marked deepening of the thermocline. The best correlation with the 20°C isotherm depth is for the first meridional mode Rossby wave ($r = 0.82$, significant at the 95% level). The second meridional mode Rossby wave signal does not correlate well with the 20°C isotherm depth, although the broad negative anomalies during October may explain the time lag in the isotherm depth anomalies relative to the first meridional mode Rossby wave signal earlier in October. The third meridional mode is poorly correlated with the 20°C isotherm depth, and higher modes are not considered (not shown).

To examine the Rossby wave signal in other variables, the mean vertical structure of each variable (Figure 5) is subtracted from the optimally interpolated Seaglider data at every depth to calculate anomalies. We then subtract the MIMOC annual cycle (with its mean first subtracted) for the relevant months (section 3). Since the Rossby wave signal varies minimally between the northern and southern end of the section (not shown), we meridionally average the subsequent anomalies. These final data can be considered as intraseasonal anomalies, since the optimal interpolation and time between sections has an effective high-frequency cutoff around 10 days, and the effective low-resolution cutoff is set at 95 days (the length of the data set) by the removal of the time-mean.

The derived anomalies of Seaglider temperature, salinity, density, and oxygen are shown in Figure 8. Due to the agreement of the thermocline variability with the intraseasonal Rossby wave amplitude (Figure 7a), it is likely that a large proportion of the intraseasonal variability shown here is due to Rossby waves, especially around the thermocline. In all fields, the strongest temporal variability is between the surface and 200 m depth, but there is substantial temporal variability that extends down to 1000 m. In the deeper ocean, the anomalies are often tilted (particularly for temperature (Figure 8a)), with individual contours sloping upwards with time. Upwards propagation of anomalies implies upward phase propagation in a wave framework. Upward phase propagation is consistent with downward propagation of energy associated with Rossby waves, and supports the notion that these deep anomalies are due, at least in part, to Rossby waves. However, vertically uniform anomalies are also seen, especially in the upper ocean. It is likely that the complex vertical structure and vertical propagation speeds are indicative of the superposition of multiple baroclinic modes. These deep ocean wave signals are similar to the deep ocean Kelvin waves forced by the MJO [*Matthews et al*., 2007, 2010] and underline the influence that the MJO has on deep ocean variability. However, a key difference from those studies of Kelvin waves is the meridional advection that will be induced by the meridional velocity anomalies associated with Rossby waves, particularly in the presence of strong meridional gradients.

For comparison with the observed anomalies, we calculate the theoretical vertical structure of the pressure anomalies (equivalent to the variables analyzed here), along with the vertical velocity anomalies for the first five baroclinic modes for the measured density stratification (Figure 9). The first mode (black line) shows anomalies of uniform sign throughout the top 1000 m. Coupled with vertical propagation, this mode can

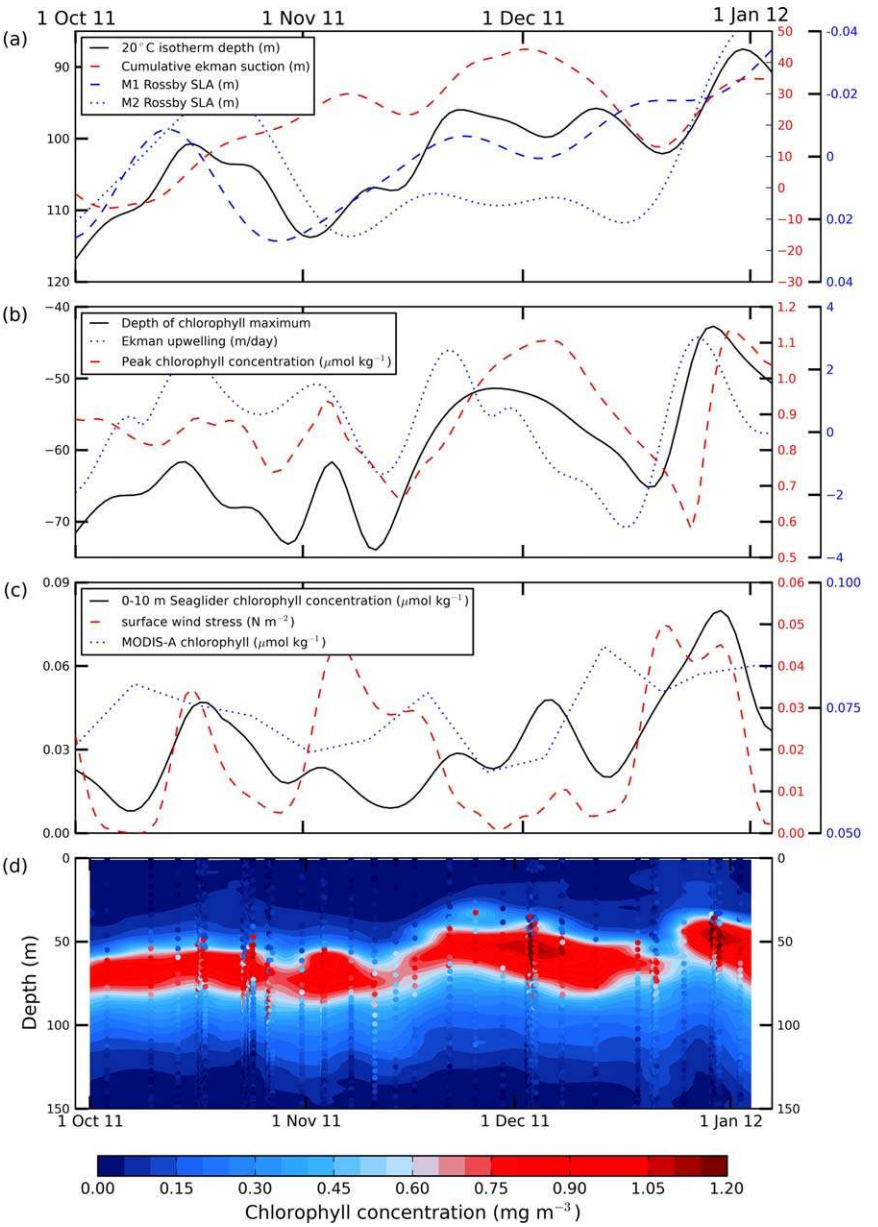

Figure 7. (a) Depth of 20°C isotherm (black line) and chlorophyll maximum (red dashed line) (m); inverted 20–200 day filtered SLA (m) (blue dotted line), (b) chlorophyll concentration at the chlorophyll maximum (black line) and averaged over 1–150 m (red dashed line) (mg m^{-3}); (c) 0–10 m chlorophyll concentration (black line) (mg m^{-3}), surface wind stress (red dashed line) (N m^{-2}), and chlorophyll concentration from the MODIS-A satellite data (blue dotted line) (mg m^{-3}) and, (d) gridded chlorophyll concentration (shaded; mg m^{-3}, see legend) and the corresponding ungridded observations (scattered, same color scale).

explain a large proportion of the variance observed, particularly in salinity and density; however, there is evidence for higher modes in the more complex structure near the surface. The vertical profile of the temperature anomalies at the start of January appears to be indicative of a third baroclinic mode wave, with zero crossings at around 80–600 m. However, given the relatively short record, it is not possible to more quantitatively decompose the variability into the constituent modes.

We compare the results from the Seaglider to the ECCO-JPL to investigate the degree to which this ocean state estimate reproduces the observed variability. The equivalent calculations using the ECCO-JPL ocean state estimate (removing the mean and seasonal cycle in the same way) show considerably different results (Figures 8e and f), although there are some common features. The temperature anomalies in the ECCO-JPL

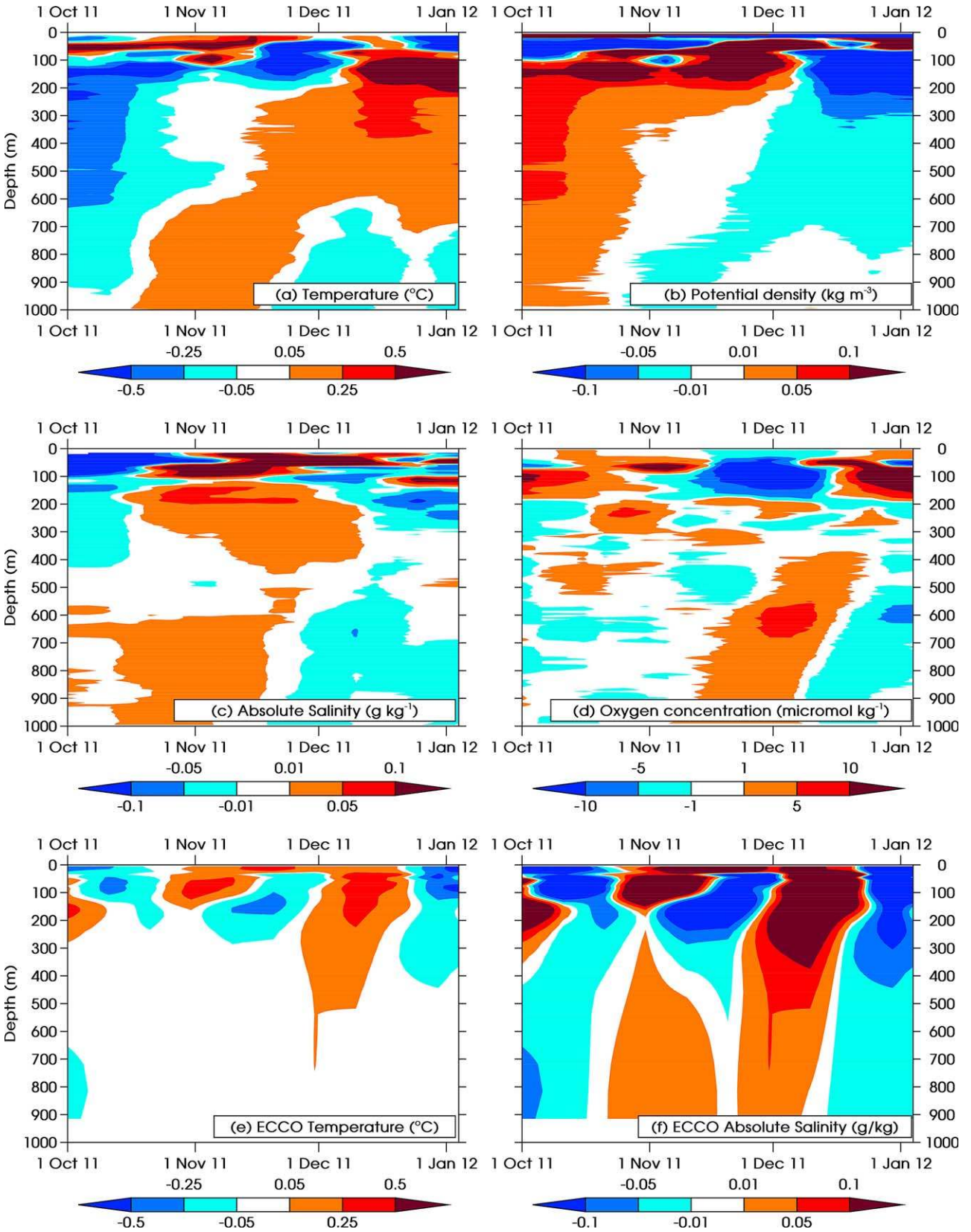

Figure 8. Latitudinal-mean sections of anomalies from the time-mean and the MIMOC annual cycle for the Seaglider data. (a) temperature (°C), (b) potential density (kg m^{-3}), (c) absolute salinity (g kg^{-1}), (d) dissolved oxygen concentration (μmol kg^{-1}), (e) ECCO-JPL temperature anomalies after removal of the time-mean and annual cycle (°C), (f) ECCO-JPL absolute salinity anomalies (g kg^{-1}).

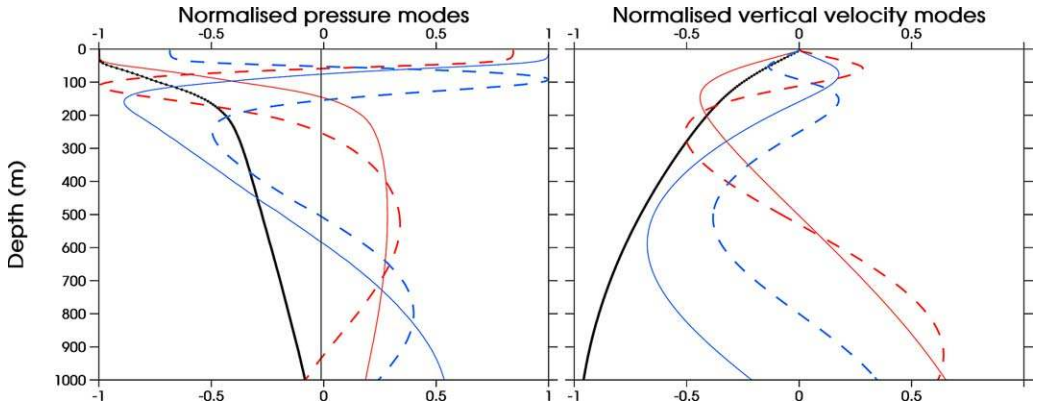

Figure 9. Theoretical baroclinic modes of (left) pressure and (right) vertical velocity anomalies calculated from the observed density stratification, extended using World Ocean Atlas data beneath 1000 m. First mode = black solid line, second= red solid line, third = blue solid line, fourth = red dashed line; fifth = blue dashed line.

data are largely confined to the upper 300 m, with minimal anomalies below this depth, while the salinity anomalies are of a much larger magnitude than in the Seaglider observations. These differences may be due to an inadequate resolution of small-scale features in the equatorial current systems in the ECCO data, since the spatial resolution is only 1°. In addition, the subsurface observations assimilated into the ECCO model are sparsely distributed, reducing the reliability of the state estimate.

5.2. Vertical Displacement and Velocities

As equatorial Rossby waves are associated with a pattern of vertical motion, an interpretation of the observed anomalies is sought in terms of vertical displacements in the presence of a mean vertical gradient. Hence, we calculate the vertical displacement anomaly (Z') associated with the observed temperature anomalies as follows:

$$Z' = -\frac{T'}{\left(\frac{d\bar{T}}{dZ}\right)}, \tag{5}$$

where T' is the temperature anomaly calculated by subtracting the annual cycle and the mean residual (Figure 8a), and $\frac{d\bar{T}}{dZ}$ is the mean vertical temperature gradient (red dashed line in Figure 5a). In this analysis, contributions to Z' from horizontal advection, surface fluxes, and entrainment are all neglected. The calculated depth anomalies (Figure 10a) are of the order of 10 m, increasing with depth. This increase with depth is consistent with the first baroclinic mode (Figure 9b), but the sign reversals around 200 m indicate the presence of higher modes. The anomalies at around 100 m exhibit the same temporal variability as the 20°C isotherm, and are also consistent with the Rossby wave signal in the altimetry data. That these are often out of phase with the anomalies at greater depths suggests either vertical propagation or the existence of higher baroclinic modes. The magnitude and sign of these vertical displacement anomalies are consistent with the results of *Matthews et al*. [2010], who found anomalies of 8 m at 1400 dbar associated with equatorial Kelvin waves. These results are also comparable to those of *McCreary* [1993], who found vertical displacements of around 20 m associated with the annual Rossby wave signal in the Pacific.

It is also possible that horizontal advection contributes to the temperature anomalies observed. Calculations based on the mean *meridional* temperature gradient and the observed anomalies (similar to equation (5)) suggest that the horizontal displacement required to produce the observed anomalies would be of the order of 100 km at around 500 m depth, which is similar to the meridional scale of Rossby waves. However, the mean meridional temperature gradient changes sign at 800 m, which is not observed in the anomalies. Therefore, to explain the observed anomalies, we would have to invoke meridional currents with a zero crossing at this depth. This is not consistent with the vertical structure of any of the first five baroclinic modes. It is therefore more logical that the anomalies observed are generated predominantly by vertical advection. In addition, positive temperature anomalies often coincide with negative salinity anomalies in

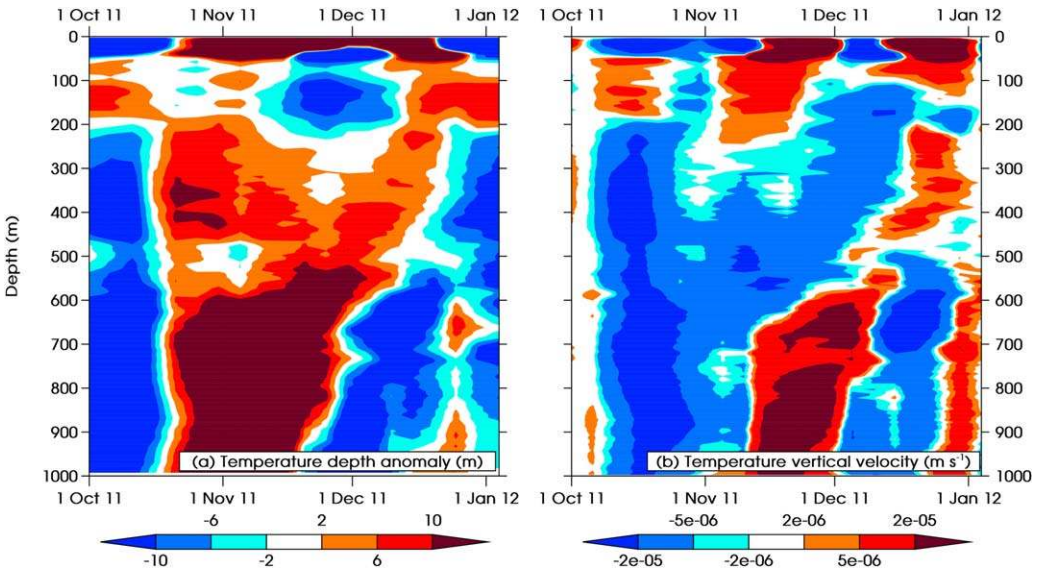

Figure 10. (a) Depth-anomaly (m) calculated from the latitudinal-mean temperature anomalies and the mean temperature structure, (b) the resulting vertical velocity anomalies (m s^{-1}).

the top 200 m; this is unlikely to be associated with meridional advection since the meridional gradient is positive for both temperature and salinity.

Assuming the temperature anomalies are due to vertical advection, equation (5) can be differentiated to give an estimation of the vertical velocity anomalies w':

$$w' = -\left(\frac{dT'}{dt} \Big/ \frac{d\bar{T}}{dz}\right). \tag{6}$$

Vertical velocity anomalies (Figure 10b) reach magnitudes of 2×10^{-5} m s^{-1}, or 1.7 m d^{-1}, and are also typically greater at depth. Even taking into account the possibility that these are overestimated due to horizontal advection, these velocity anomalies are a substantial addition to the deep ocean variability in this region.

The dissolved oxygen concentration exhibits considerable variability (Figure 8d). In the top 200 m, this variability is positively correlated with temperature variability and negatively correlated with salinity variability, indicating a role for vertical displacement, since negative temperature and oxygen anomalies, and positive salinity anomalies, would indicate the presence of upwelling, and vice-versa. Also, since negative temperature anomalies coincide with positive salinity anomalies, it appears that meridional advection is not responsible for these anomalies since the meridional gradients in both temperature and salinity are positive. The oxygen concentration anomalies are larger than 10 μmol kg^{-1} at 100 m depth, consistent with vertical displacements of around 10 m given the vertical gradient at this depth (Figure 5d); this agrees with the independent estimate of vertical displacement from the temperature data. There is also likely to be a biological influence on the dissolved oxygen concentration (see section 5.3.), but this cannot be diagnosed with the available data.

5.3. Impact on Chlorophyll Concentrations

The chlorophyll data were sampled at a lower resolution than the other data sets presented here. The chlorophyll sensor was only switched on sporadically to conserve battery and due to piloting constraints these dives were often grouped together. The average gap between dives when the chlorophyll sensor was on was approximately 3 days. Due to the relatively sparse data, the optimal interpolation could not be performed on the same grid as for the other variables. Instead, the spatial information was discarded from the start, such that the data were interpolated onto a two-dimensional (depth-time) grid, with radii of influence of 5 m and 5 days, respectively.

There is a clear subsurface chlorophyll maximum between 40 and 80 m throughout the glider deployment (Figure 7d). The depth of the chlorophyll maximum was calculated from the optimally interpolated chlorophyll data (Figure 7b). There is a correlation of $r = 0.65$ between the depth of the chlorophyll maximum and the depth of the 20°C isotherm (significant at the 95% level), with stronger agreement during the latter half of the observational period. We also compute the upwelling due to local Ekman pumping, and find that this is closely related to the depth of the chlorophyll maximum; with a correlation of $r = 0.62$ at a lag of 2 days. This implies that the local upwelling is at least as important as the remotely forced upwelling in driving chlorophyll variability, perhaps because the chlorophyll maximum is shallow relative to the 20°C isotherm, and thus more susceptible to wind forcing.

The variation in peak chlorophyll concentration (Figure 5, blue dotted line) is also consistent with the Ekman-induced upwelling (maximum correlation $r = 0.61$ at a lag of one week), and consistent to a lesser degree with the Rossby wave amplitude. This suggests that increased nutrient availability associated with the upwelling encourages phytoplankton blooms. In addition, the shoaling of the chlorophyll maximum will increase light availability, also increasing productivity. The lag between the depth of the chlorophyll maximum and the peak concentration suggests a gradual blooming of the phytoplankton in response to this increased light and nutrient availability. The integrated chlorophyll concentration from the surface to 150 m is closely correlated to the peak chlorophyll concentration ($r = 0.84$; not shown), suggesting that this variability is mostly uniform over this depth range. The link to Rossby waves, although weak, suggests a dynamic role for the MJO in modulating primary productivity in this region through the generation of Rossby waves. However, the intraseasonal wind variability, also associated with the MJO, appears to be the primary driver of chlorophyll variability at the deep chlorophyll maximum.

Chlorophyll data derived from ocean colour observations from the Moderate Resolution Imaging Spectroradiometer (MODIS) on the Aqua spacecraft (blue dotted line, Figure 7c) were compared with the Seaglider estimates of chlorophyll fluorescence from the Wetlabs puck. We follow the methodology of *Perry et al*. [2008] in using the average chlorophyll concentration over the top 10 m from the Seaglider for the comparison (black solid line, Figure 7c). It is interesting to note that the MODIS chlorophyll data show concentrations that are around twice as large as the Seaglider estimate, but with much reduced variability compared with the Seaglider data. *Perry et al*. [2008] also observed discrepancies between Seaglider-observed chlorophyll and satellite data, concluding that the absolute values observed by Seagliders may be too high, but that the temporal and spatial variability are robust. Since we are concerned with the variability of the chlorophyll in the context of Rossby waves, our conclusions are unaffected by a constant offset.

The peaks in near-surface chlorophyll (black line, Figure 7c) in mid-October, early and late December could be partially attributed to upwelling, particularly the peak in late December. The first and last peaks correspond to shoaling of the 20°C isotherm, as well as increased surface wind stress. The peak in early December lags the shoaling of the 20°C isotherm, but coincides with increased chlorophyll concentrations at the deep chlorophyll maximum. Previous studies have found correlations between surface wind stress and surface chlorophyll [e.g., *Waliser et al*., 2005] with enhanced surface wind stress leading to higher surface chlorophyll through enhanced mixing up of chlorophyll and nutrients from below. Our results suggest that peaks in surface wind stress derived from ERA-interim data (red line in Figure 7c) are sometimes, but not always, associated with peaks in surface chlorophyll, suggesting a combination of wind stress and upwelling may drive the variability in surface chlorophyll.

6. Conclusions

A Seaglider was deployed for 4 months in the Indian Ocean, and patrolled between 3 and 4°S for 95 days between 1 October 2011 and 4 January 2013, collecting temperature, salinity, dissolved oxygen, and chlorophyll-*a* fluorescence data. These data show the mean vertical hydrographic structure of this region of the Indian Ocean and the temporal variability induced primarily by intraseasonal Rossby waves.

A key result of this paper is that we are able to identify equatorial ocean Rossby waves in subsurface data measured by an ocean glider. This identification was through projection of the intraseasonal SLA onto theoretical Rossby wave structures and comparison of this signal against the thermocline and pycnocline variability observed by the Seaglider, which mirrors the variability in the sea surface. Analysis of the wind field compared with the SLA suggests that these waves were associated with the MJO activity during the

CINDY–DYNAMO period, partly through westerly wind forcing of Kelvin waves, and partly through direct forcing by the wind stress curl. The anomalies associated with Rossby waves in temperature, salinity, density, and dissolved oxygen observed by the Seaglider were substantial compared with the annual cycle in the deep ocean (>500 m) and found to be coherent to 1000 m, the greatest depth observed here. That a significant signal is observed in the deep ocean confirms previous work on the role of the MJO in generating deep ocean variability near the equator [*Matthews et al*., 2007, 2010].

Estimates of vertical displacements from the temperature data show vertical displacements of greater than 10 m, with the biggest displacements occurring at 1000 m depth, consistent with previous observations of annual Rossby waves [*McCreary*, 1993; *Johnson*, 2011]. The time evolution of these anomalies suggests vertical velocities of around 1 m day^{-1}, although this could be biased high if meridional advection is a major driver of the observed temperature anomalies. The amplitude of these displacements is around 20% of the variability in isopycnal depth in the annual cycle, but the relatively short time scales mean the vertical velocities are of similar magnitude to the annual cycle [c.f., *Johnson*, 2011]. Meridional advection is also likely to account for some of the variability, especially in salinity and oxygen, which have large meridional gradients, and particularly at intermediate depths below the main halocline and oxycline at depths where the meridional gradients are large.

The chlorophyll data show a strong relationship between the upwelling induced by the curl of the intraseasonal wind stress and the depth of the chlorophyll maximum, as well as peak and integrated chlorophyll concentration. This is indicative of a role for increased light and nutrient availability associated with upwelling (and vice-versa), as well as vertical displacement of the chlorophyll. These chlorophyll variations are unlikely to be due to Rossby wave-driven particle convergence, since we do not find peaks in surface backscatter associated with downwelling Rossby wave signals. There also appears to be a role for the Rossby waves in modulating both the depth of the chlorophyll maximum and the net chlorophyll concentrations, which may also influence net carbon export. The satellite-derived chlorophyll data from MODIS-AQUA do not capture the observed chlorophyll variability, primarily because of the depth of the chlorophyll maximum (> 50 m).

The Seaglider deployment was during an intensive observational period for the CINDY–DYNAMO field campaign to study the MJO. Three MJOs occurred during this period, associated with strong westerly wind bursts that in turn triggered a substantial amount of Rossby wave activity, and the resultant Rossby waves have been observed by the Seaglider. The last of these three MJO events triggered a downwelling Rossby wave that subsequently may have had a role in triggering the very strong MJO event that began in mid-February 2012.

Acknowledgments

The research leading to these results has received funding from the European Union 7th Framework Programme (FP7 2007-2013) under grant agreement 284321 GROOM Project. The Seaglider deployment would not have been possible without the support from crew and scientists aboard the RV Roger Revelle. The altimeter products were produced by SSALTO/DUACS and distributed by AVISO with support from CNES and are available online at www.aviso.oceanobs.com/. The EMCWF surface wind data were obtained through the British Atmospheric Data Centre (BADC) and from the ECMWF website at data-http://apps.ecmwf.int/datasets/data/interim_full_daily/. The interpolated OLR data were obtained from the NOAA/OAR/ESRL PSD website at www.cdc.noaa.gov/. Data from the ECCO-JPL project were obtained from ecco.jpl.nasa.gov/. We thank two anonymous reviewers whose comments helped to greatly improve the manuscript.

References

Bretherton, F. P., R. E. Davis, and C. Fandry (1976), A technique for objective analysis and design of oceanographic experiments applied to mode-73, *Deep Sea Res. Oceanogr. Abstr.*, *23*, 559–582.

Chelton, D. B., R. A. DeSzoeke, M. G. Schlax, K. El Naggar, and N. Siwertz (1998), Geographical variability of the first baroclinic Rossby radius of deformation, *J. Phys. Oceanogr.*, *28*(3), 433–460.

Dandonneau, Y., A. Vega, H. Loisel, Y. Du Penhoat, and C. Menkes (2003), Oceanic Rossby waves acting as a "hay rake" for ecosystem floating by-products, *Science*, *302*(5650), 1548–1551.

Dandonneau, Y., P.-Y. Deschamps, J.-M. Nicolas, H. Loisel, J. Blanchot, Y. Montel, F. Thieuleux, and G. Bécu (2004), Seasonal and interannual variability of ocean color and composition of phytoplankton communities in the North Atlantic, equatorial Pacific and South Pacific, *Deep Sea Res. Part II*, *51*(1), 303–318.

Dee, D. P., et al. (2011), The ERA-Interim reanalysis: Configuration and performance of the data assimilation system, *Q. J. R. Meteorol. Soc.*, *137*(656, Part a), 553–597, doi:10.1002/qj.828.

Delcroix, T., J.-P. Boulanger, F. Masia, and C. Menkes (1994), Geosat-derived sea level and surface current anomalies in the equatorial Pacific during the 1986–1989 El Niño and La Niña, *J. Geophys. Res.*, *99*(C12), 25,093–25,107.

Eriksen, C., T. Osse, R. Light, T. Wen, T. Lehman, P. Sabin, J. Ballard, and A. Chiodi (2001), Seaglider: A long-range autonomous underwater vehicle for oceanographic research, *IEEE J. Oceanic Eng.*, *26*(4), 424–436.

Frajka-Williams, E., C. C. Eriksen, P. B. Rhines, and R. R. Harcourt (2011), Determining vertical water velocities from Seaglider, *J. Atmos. Oceanic Technol.*, *28*(12), 1641–1656, doi:10.1175/2011JTECHO830.1.

Fu, L. L., E. J. Christensen, C. A. Yamarone, M. Lefebvre, Y. Menard, M. Dorrer, and P. Escudier (1994), TOPEX/Poseidon mission overview, *J. Geophys. Res.*, *99*(C12), 24,369–24,381.

Fu, X., J.-Y. Lee, P.-C. Hsu, H. Taniguchi, B. Wang, W. Wang, and S. Weaver (2013), Multi-model MJO forecasting during dynamo/cindy period, *Clim. Dyn.*, *41*(3-4), 1067–1081.

Gottschalck, J., P. E. Roundy, C. J. Schreck III, A. Vintzileos, and C. Zhang (2013), Large-scale atmospheric and oceanic conditions during the 2011-12 dynamo field campaign, *Mon. Weather Rev.*, *141*(12), 4173–4196.

Han, W., D. M. Lawrence, and P. J. Webster (2001), Dynamical response of equatorial Indian Ocean to intraseasonal winds: Zonal flow, *Geophys. Res. Lett.*, *28*(22), 4215–4218, doi:10.1029/2001GL013701.

Hendon, H. H., B. Liebman, and J. D. Glick (1998), Oceanic Kelvin waves and the Madden Julian oscillation, *J. Atmos. Sci.*, *55*, 88–101, doi:Url link having entity. Please change to keyboard character....10.1175/1520-0469(1998)055¡0088:OKWATM¿2.0.CO;2.

Heywood, K., E. Barton, and G. Allen (1994), South equatorial current of the Indian-Ocean-a 50-day oscillation, *Oceanol. Acta*, *17*(3), 255–261.

IOC, SCOR, IAPSO (2010), *The International Thermodynamic Equation of Seawater—2010: Calculation and Use of Thermodynamic Properties*, UNESCO (English), 220 pp., Intergovernmental Oceanographic Commission, United Nations Educational, Scientific and Cultural Organization, Paris, France.

Johnson, G. C. (2011), Deep signatures of southern tropical Indian ocean annual Rossby waves, *J. Phys. Oceanogr.*, *41*(10), 1958–1964.

Kessler, W. S., and M. J. McPhaden (1995), Oceanic equatorial waves and the 1991-93 El-Nino, *J. Clim.*, *8*(7), 1757–1774.

Kessler, W. S., M. J. McPhaden, and K. M. Weickmann (1995), Forcing of intraseasonal Kelvin waves in the equatorial pacific, *J. Geophys. Res.*, *100*(C6), 10,613–10,631, doi:10.1029/95JC00382.

Lau, W. K. M., and D. E. Waliser (Eds.) (2005), *Intraseasonal Variability in the Atmosphere–Ocean Climate System*, 436 pp., Springer-Praxis, Heidelberg, Germany.

Liebmann, B., and C. A. Smith (1996), Description of a complete (interpolated) outgoing longwave radiation dataset, *Bull. Am. Meteorol. Soc.*, *77*(6), 1275–1277.

Madden, R. A., and P. R. Julian (1971), Detection of a 40-50 day oscillation in zonal wind in the tropical Pacific, *J. Atmos. Sci.*, *28*(5), 702–708.

Madden, R. A., and P. R. Julian (1972), Description of global-scale circulation cells in the tropics with a 40–50 day period, *J. Atmos. Sci.*, *29*(6), 1109–1123.

Matthews, A. J., P. Singhruck, and K. J. Heywood (2007), Deep ocean impact of a Madden-Julian oscillation observed by Argo floats, *Science*, *318*, 1765–1768, doi:10.1126/science.1147312.

Matthews, A. J., P. Singhruck, and K. J. Heywood (2010), Ocean temperature and salinity components of the Madden-Julian oscillation observed by Argo floats, *Clim. Dyn.*, *35*(7–8), 1149–1168, doi:10.1007/s00382-009-0631-7.

McCreary, J. P. (1983), A model of tropical ocean-atmosphere interaction, *Mon. Weather Rev.*, *111*(2), 370–387.

McCreary, J. P. (1993), The annual wind-driven Rossby wave in the subthermocline equatorial Pacific, *J. Phys. Oceanogr*, *23*, 1192–1207.

McPhaden, M. J. (1999), Genesis and evolution of the 1997–98 El niño, *Science*, *283*, 950–954, doi:10.1126/science.283.5404.950.

Morison, J., R. Andersen, N. Larson, E. D'Asaro, and T. Boyd (1994), The correction for thermal-lag effects in Sea-Bird CTD data, *J. Atmos. Oceanic. Technol.*, *11*(4), 1151–1164.

Moum, J. N., et al. (2013), Air-sea interactions from westerly wind bursts during the November 2011 MJO in the Indian ocean, *Bull. Am. Meteorol. Soc.*, doi:10.1175/BAMS-D-12-00225.1.

Oliver, E. C. J., and K. R. Thompson (2010), Madden-Julian Oscillation and sea level: Local and remote forcing, *J. Geophys. Res.*, *115*, C01003, doi:10.1029/2009JC005337.

Perry, M., B. Sackmann, C. Eriksen, and C. Lee (2008), Seaglider observations of blooms and subsurface chlorophyll maxima off the Washington coast, *Limnol. Oceanogr.*, *53*(2), 2169–2179.

Rudnick, D. L., and S. T. Cole (2011), On sampling the ocean using underwater gliders, *J. Geophys. Res.*, *116*, C08010, doi:10.1029/2010JC006849.

Salby, M. L., and H. H. Hendon (1994), Intraseasonal behavior of clouds, temperature, and motion in the tropics, *J. Atmos. Sci.*, *51*(15), 2207–2224.

Schmidtko, S., G. C. Johnson, and J. M. Lyman (2013), MIMOC: A global monthly Isopycnal Upper-ocean climatology with mixed layers, *J. Geophys. Res., Ocean 118*, 1658–1672, doi:10.1002/jgrc.20122.

Shinoda, T., T. G. Jensen, M. Flatau, S. Chen, W. Han, and C. Wang (2013), Large-scale oceanic variability associated with the Madden-Julian oscillation during the cindy/dynamo field campaign from satellite observations, *Remote Sens.*, *5*(5), 2072–2092.

Talley, L. D., G. L. Pickard, W. J. Emery, and J. H. Swift (2011), *Descriptive Physical Oceanography: An Introduction*, Academic, Academic Press, London, U. K.

Uz, B. M., J. A. Yoder, and V. Osychny (2001), Pumping of nutrients to ocean surface waters by the action of propagating planetary waves, *Nature*, *409*(6820), 597–600.

Waliser, D. E., R. Murtugudde, P. Strutton, and J. L. Li (2005), Subseasonal organization of ocean chlorophyll: Prospects for prediction based on the Madden-Julian Oscillation, *Geophys. Res. Lett.*, *32*, L23602, doi:10.1029/2005GL024300.

Webber, B. G. M., A. J. Matthews, and K. J. Heywood (2010), A dynamical ocean feedback mechanism for the Madden-Julian oscillation, *Q. J. R. Meteorol. Soc.*, *136*(648, Part A), 740–754, doi:10.1002/qj.604.

Webber, B. G. M., A. J. Matthews, K. J. Heywood, and D. P. Stevens (2012a), Ocean Rossby waves as a triggering mechanism for primary Madden-Julian events, *Q. J. R. Meteorol. Soc.*, *138*, 514–527, doi:10.1002/qj.936.

Webber, B. G. M., D. P. Stevens, A. J. Matthews, and K. J. Heywood (2012b), Dynamical ocean forcing of the Madden-Julian oscillation at lead times of up to five months, *J. Clim.*, *25*(8), 2824–2842, doi:10.1175/JCLI-D-11–00268.1.

Wunsch, C., and P. Heimbach (2007), Practical global oceanic state estimation, *Physica D*, *230*(1-2), 197–208, doi:10.1016/j.physd.2006.09.040.

Yoneyama, K., C. Zhang, and C. N. Long (2013), Tracking pulses of the Madden-Julian oscillation, *Bull. Am. Meteorol. Soc.*, *94*, 1871–1891, doi:10.1175/BAMS-D-12–00157.1.

Zhang, C. D. (2005), Madden-Julian oscillation, *Rev. Geophys.*, *43*, RG2003, doi:10.1029/2004RG000158.